Evaporation-Induced Composition Evolution in Metal Additive Manufacturing

Wang, Lu; Guo, Zixu; Peng, Guochen; Wu, Shiwei; Zhang, Yanming; Yan, Wentao

Published in:
Advanced Functional Materials

Published: 12/02/2025

Document Version:
Final Published version, also known as Publisher's PDF, Publisher's Final version or Version of Record

Published version (DOI):
10.1002/adfm.202412071

Publication details:
Wang, L., Guo, Z., Peng, G., Wu, S., Zhang, Y., & Yan, W. (2025). Evaporation-Induced Composition Evolution in Metal Additive Manufacturing. *Advanced Functional Materials*, *35*(7), Article 2412071. https://doi.org/10.1002/adfm.202412071

ADVANCED FUNCTIONAL MATERIALS
www.afm-journal.de

Evaporation-Induced Composition Evolution in Metal Additive Manufacturing

*Lu Wang, Zixu Guo, Guochen Peng, Shiwei Wu, Yanming Zhang, and Wentao Yan**

In fusion-based metal additive manufacturing (MAM), the high-intensity energy input leads to serious evaporation, but how evaporation induces composition evolution and variation and further impacts microstructure and mechanical properties remain a knowledge gap. Here a model integrating composition evolution with molten pool dynamics is developed to reproduce temperature- and composition-dependent evaporative losses and subsequent transport during laser melting. Together with comprehensive experimental characterizations and tests, the simulation results illustrate varying evaporation rates of different elements altering compositions, resulting in a 3D cirrus-shaped concentration distribution, which significantly impacts the mechanical properties. The simulations reproduce the detailed composition evolution from surface evaporation to molten pool transport and reveal underlying mechanisms relating the composition, temperature, fluid flow, and cracking, which is challenging to observe experimentally. This study elucidates the critical role of evaporation-induced composition evolution in determining microstructure and mechanical properties. In future alloy design for MAM, integrating initial composition and manufacturing parameters is imperative, where composition evolution simulation offers valuable guidance.

1. Introduction

Fusion-based metal additive manufacturing (MAM),[1–4] e.g., laser powder bed fusion (L-PBF), has gained significant attention in various industries such as aerospace, automobile, and biomedical engineering, due to its capability to fabricate intricate components with high strength. Compared to traditional manufacturing processes, the tiny-size high-energy density heat source in fusion-based MAM processes induces high cooling rates[5,6] and large temperature gradients,[7,8] which effectively decrease grain sizes and improve the mechanical properties of the as-built parts.[2,7] However, the heat source also results in serious metal evaporation,[9,10] altering the compositions by burning off the volatile elements.[11–13] Recent ex situ studies[14–23] found that the evaporation-induced composition variation will influence phase transformation, change the grain morphology and mechanical property under different processing parameters. Under the combined effect of the local temperature history and element concentration variation, the dendrite/grain growth becomes more complicated, even leading to cracking.[24] However, there are no effective solutions to control element evaporation and optimize the component composition to improve the quality consistency of components. Because the underlying physical mechanisms of how evaporation induces composition evolution and variation and further impacts microstructure and mechanical properties remain unclear.

The composition evolution in MAM is very complex for the following reasons: 1) the boiling temperatures of different elements in alloys vary, 2) the temperature at the molten pool/keyhole surface varies, and 3) the fierce molten pool flow, keyhole fluctuation, and layer-by-layer remelting further impact the element concentration distribution in the local molten pool and global as-built part.[11,14] Although inspiring progress has been achieved on in situ X-ray imaging of the molten pool flow, keyhole dynamics, and vapor flow[25–27] via 2D projections, it is still very challenging if not impossible to directly measure/characterize the local element evaporation, and composition evolution in the molten pool in three dimensions (3D) during such a short solidification period (on the order of ten microseconds) with a spatial resolution of several micrometers. While computational modeling has proven very powerful in understanding various phenomena in MAM, such as keyhole pores, spattering and solidification,[28–30] the thermal-fluid flow models incorporating both the evaporative element loss and liquid flow simultaneously hitherto are not available, which makes it very difficult to analyze the evaporation-induced composition evolution in the molten pool.

L. Wang
Department of Mechanical Engineering
College of Engineering
City University of Hong Kong
Kowloon Tong, Kowloon, Hong Kong 999077, China
Z. Guo, G. Peng, S. Wu, Y. Zhang, W. Yan
Department of Mechanical Engineering
National University of Singapore
Singapore 117575, Singapore
E-mail: mpeyanw@nus.edu.sg

The ORCID identification number(s) for the author(s) of this article can be found under https://doi.org/10.1002/adfm.202412071

DOI: 10.1002/adfm.202412071

To systematically study this critical issue, we develop a novel multi-physics thermal-fluid flow model incorporating the evaporative element loss and convection-dominated compositional evolution, and conduct a series of experiments. As the second most used alloy after steel, aluminum alloys play an important role in the aerospace industry, and become popular in MAM in the last 15 years.[24,31,32] Specifically, a representative alloy with elements of largely different boiling points, AA7075 (boiling points of Zn and Al are 1180 and 2790 K) is selected as a model material, and L-PBF is selected as a representative MAM technique, while this model is generally applicable to various materials and MAM techniques. To reduce the influence of powder particles, we use bare plates, and to strengthen the composition distribution pattern, the tracks are melted and remelted on bare plates by scanning laser for experimental characterization and simulation validation. Due to the limited experimental resources and material property data, this study mainly focuses on laser powder-bed fusion additive manufacturing and two representative alloys: AA7075 and FeMnCoCr high entropy alloy. The non-uniform element concentration distribution is extracted and analyzed combining ex situ experiments and molten pool simulation, and its impact on the mechanical property is unveiled with both micro-pillar compression tests and constitutive model. To thoroughly understand the mechanisms of composition evolution, the molten pool dynamics are elaborated in detail, from surface evaporation rate and temperature distribution to element transport with liquid flow. Leveraging the in situ X-ray imaging results of cracking formation and simulated temperature gradient and cooling rate, we find that element concentration evolution in the molten pool, especially with bubble flow, is a significant factor affecting cracking, but has never been mentioned before. This study has shed unprecedented insights into the evaporation-induced composition evolution, and can provide valuable guidance to integrate the design of powder compositions and selection of AM parameters, facilitating the development of advanced alloys.

2. Results and Discussion

2.1. Composition Variation

As schematically shown in **Figure 1a**, the compositions of vapor are not necessarily the same as those of the raw material due to the different evaporation rates of different elements (Element A and B), altering the element concentrations on the molten pool surface, which further leads to non-uniform composition in the molten pool by convection. To elucidate these complicated phenomena, we develop a compositional evolution model by incorporating the local temperature- and composition-dependent volatile element evaporation and the subsequent mass transport with convection in the molten pool flow as described in Section Compositional Evolution Model. To simulate this process during MAM, low-boiling-point elements, i.e., Zn (T_b = 1180 K) and Mg (T_b = 1363 K) in AA7075, are considered as the solute in the model. Since the reduction of Mg concentration shares a similar pattern but is less than that of Zn (as proved in Figure 1f,g), the results of Zn concentrations are mainly illustrated to analyze the composition evolution in the molten pool, where the cross section of molten pool of Case 1 (270 W, 1000 mm s^{-1}) are presented in Figure 1b–e, and Cases 2 (330 W, 1000 mm s^{-1}) and 3 (270 W, 500 mm s^{-1}) are presented in Figures S1 and S2 (Supporting Information). With the increase in laser energy density, the molten pool transitions from shallow (Case 1) to deep keyhole mode (Case 3). The molten pool dimensions in the experimental and simulation results are close (Figure 1b–e; Figures S1 and S2, Supporting Information), with relative differences below 18%. Compared to the experiments, the uncertainty of material properties (e.g., viscosity, surface tension, thermal conductivity, specific heat, etc.), real processing parameters (e.g., laser power, diameter, and defocusing), and laser attenuation by the vapor plume are not considered in the simulations due to the lack of related data. Moreover, the oxidation of the bare plate (after polishing) decreases the wettability[33,34] and influences the laser absorption and element evaporation. With these factors, the multiphysics thermal-fluid flow simulation results, with relative errors in the molten pool dimensions against the experiments being less than 18%, is considered fairly accurate. Counter-intuitively, the depth of the molten pool in remelting decreases slightly compared to that of first melting, especially under high energy density (Case 3, Figure S2c, Supporting Information). This is caused by the reduction of Zn and Mg, which in turn increases the boiling point of the alloy, and reduces the recoil pressure by evaporation in the remelting process.

Electron Probe Micro Analysis (EPMA) and simulation results quantitatively present the Zn concentration distribution in the molten pool. Overall, the Zn concentration measured by EPMA in Figure 1b,d shares a similar segregation trend as simulation results (Figure 1c,e), where element concentrations are segregated into upper and bottom regions (as identified by the red and white circles in Figure 1b,c), and the range closely matches the simulation results, 3.5–5.8 wt.% in the first melt track and 3.0–5.8 wt.% in the remelted track. Despite the volatile elements evaporation on the surface, the low Zn concentration does not appear in the middle upper region of the melt region, but instead distributes near molten pool boundaries. In the upper region, the low-Zn-concentration regions extend from the edges and infiltrate inward as shown in Figure 1b,c. In the bottom region, Zn concentration (Figure 1b,c) close to the boundary is lower (black dashed circles) at ≈4 wt.%. Moreover, in the remelted track (Figure 1d,e), the concentration at the edge and the middle of the tracks decreases further compared to that in the first melt track (Figure 1b,c), and the lower limit of Zn concentration decreases from 3.5 to 3.0 wt.% due to the further element evaporation and liquid convection. At the same time, the Zn segregation in the upper and bottom regions in both EPMA and simulation results become more obscured after remelting, as shown in Figure 1d,e. In the simulation, the drag force in the mushy zone is assumed to be isotropic. However, since the grain morphology is mostly columnar and rarely equiaxed, the drag force in the mushy zone is actually anisotropic. Moreover, micropores in the substrate influence the molten pool flow, leading to more significant concentration deviations in the first track, as shown in Figure 1c, when compared to EPMA results. As remelting time increases, these concentration deviations decrease, as illustrated in Figure 1d,e. To enhance the accuracy of simulation in future studies, the drag force model should be revised to account for grain morphology.

It should be highlighted that there are discernible concentration differences in different cross sections, as shown in

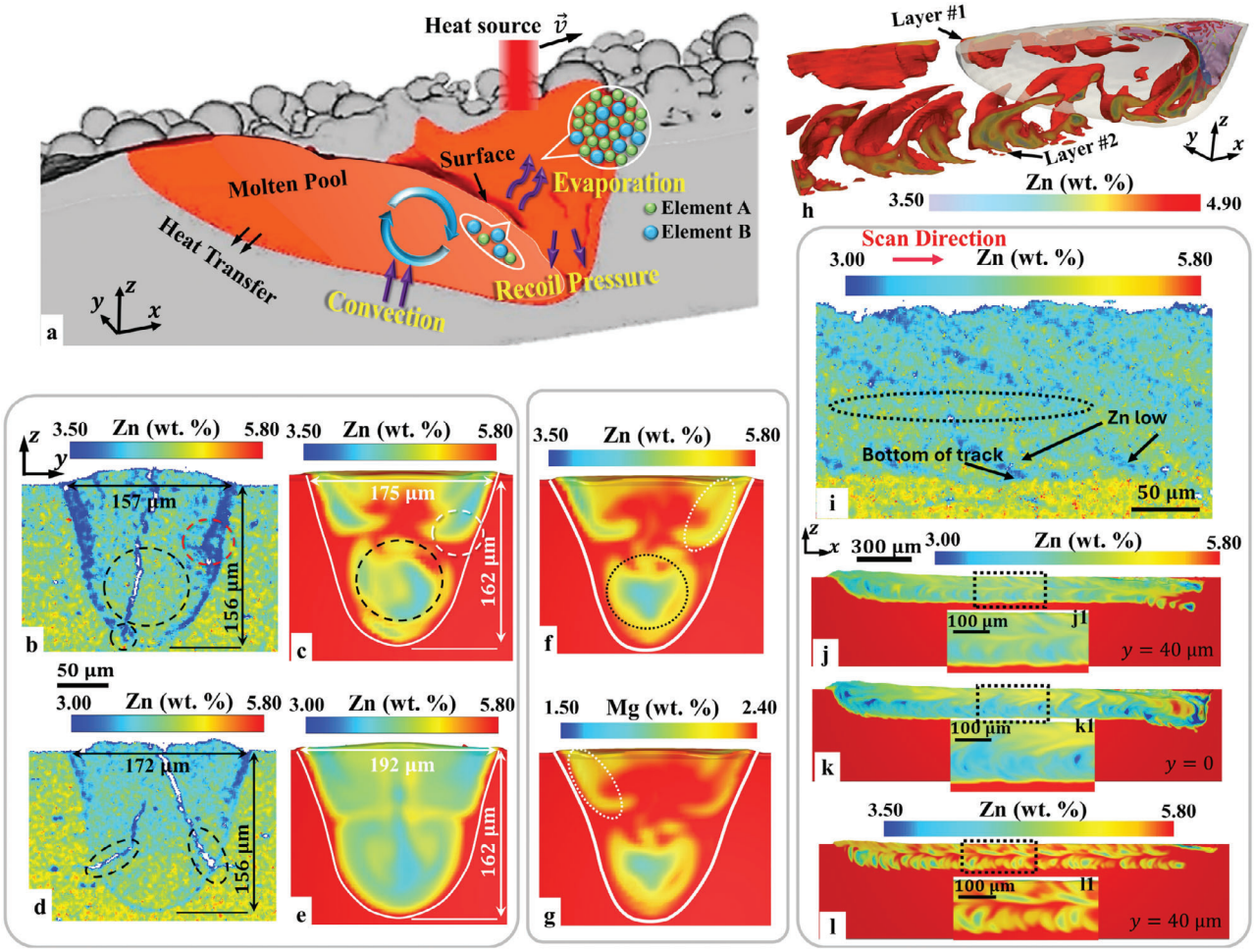

Figure 1. Evaporation-induced compositional variation. a) Schematic of composition evolution in the molten pool. b,c and f,g) and d,e) are the results of the first melt and remelted (Time interval after the first melting is 120 s) tracks in Case 1 (270 W, 1000 mm s^{-1}). (b and d) The Wiener filtered EPMA results. (c and e–g) Simulation results. The red and black circles in (b) indicate regions with lower Zn concentrations. Red and white circles in (b) and (c) indicate the concentration segregating into upper and bottom regions. Black circles in (b,c) and (f) indicate the Zn mixing process at the bottom of the molten pool. Black circles in (d) indicate that cracks hinder the concentration mixing at the bottom of the molten pool. (f) Zn and (g) Mg concentration distributions in another cross section in Case 1, which is 110 μm apart from (c). The dashed circle and ellipse in (f,g) indicate different element concentrations from (c). The fusion zone boundaries are marked by the white solid lines in (c and e–g). h) 3D cirrus-shaped distributed low-Zn-concentration in the track. The gray contour in (h) is the boundary of the molten pool at solidus temperature. i) The filtered EPMA results of Zn concentration in the longitudinal section (close to $y = 0$ plane) of the remelted track in Case 1. Compared to that in the first track in Figure S3 (Supporting Information), more Zn evaporates from the remelted track and it has a more obvious distribution pattern here. The Zn concentrations are intermittently distributed (indicated by the "Zn low" arrows). The Zn concentrations in the dashed elliptical regions are discontinuous indicating that the Zn concentration segregates into upper and bottom regions. The simulated Zn concentration distribution in j) longitudinal section $y = 40$ μm, k) middle longitudinal section $y = 0$ of the remelted track, and (l) longitudinal section $y = 40$ μm of the first track in Case 1. (j1–l1) are the enlarged views of black dashed rectangular regions in (j–l) for comparison to (i).

Figure 1f,g,c (just 110 μm apart in the x direction), which is also part of the reasons for the difference between EPMA and simulation results. This is because the concentration distribution is essentially in 3D, and 2D cross-section views are not fully representative. Only 3D high-fidelity simulation can provide comprehensive views of such 3D distribution (Figure 1h), while it is very challenging in experiments. The low-Zn-concentration regions (<4.9 wt%) show a 3D cirrus-shaped distribution in the bottom and upper regions of the track. Correspondingly, the Zn concentrations display intermittent patterns along the laser scanning direction in longitudinal sections (Figure 1i–l; Figure S3–S5, and Movie S1–S6, Supporting Information), similar to the Energy-Dispersive X-ray Spectroscopy (EDS) results by Yao et al.,[35] At the same time, in Figure 1i–l and Figure S3 (Supporting Information), the Zn concentration in tracks are intermittent and discontinuous along both the z (the black dashed elliptical regions in Figure 1i) direction. Since Figure 1i and Figure S3a (Supporting Information) are not exactly on $y = 0$ plane, the intermittent Zn contraction in the upper region in experiments, which is more like the Zn concentration distribution in Figure 1j,l. Moreover, compared to Zn concentration in $y = 0$ planes in Figure 1k, the Zn segregation along z direction in $y = 40$ μm planes (Figure 1j)

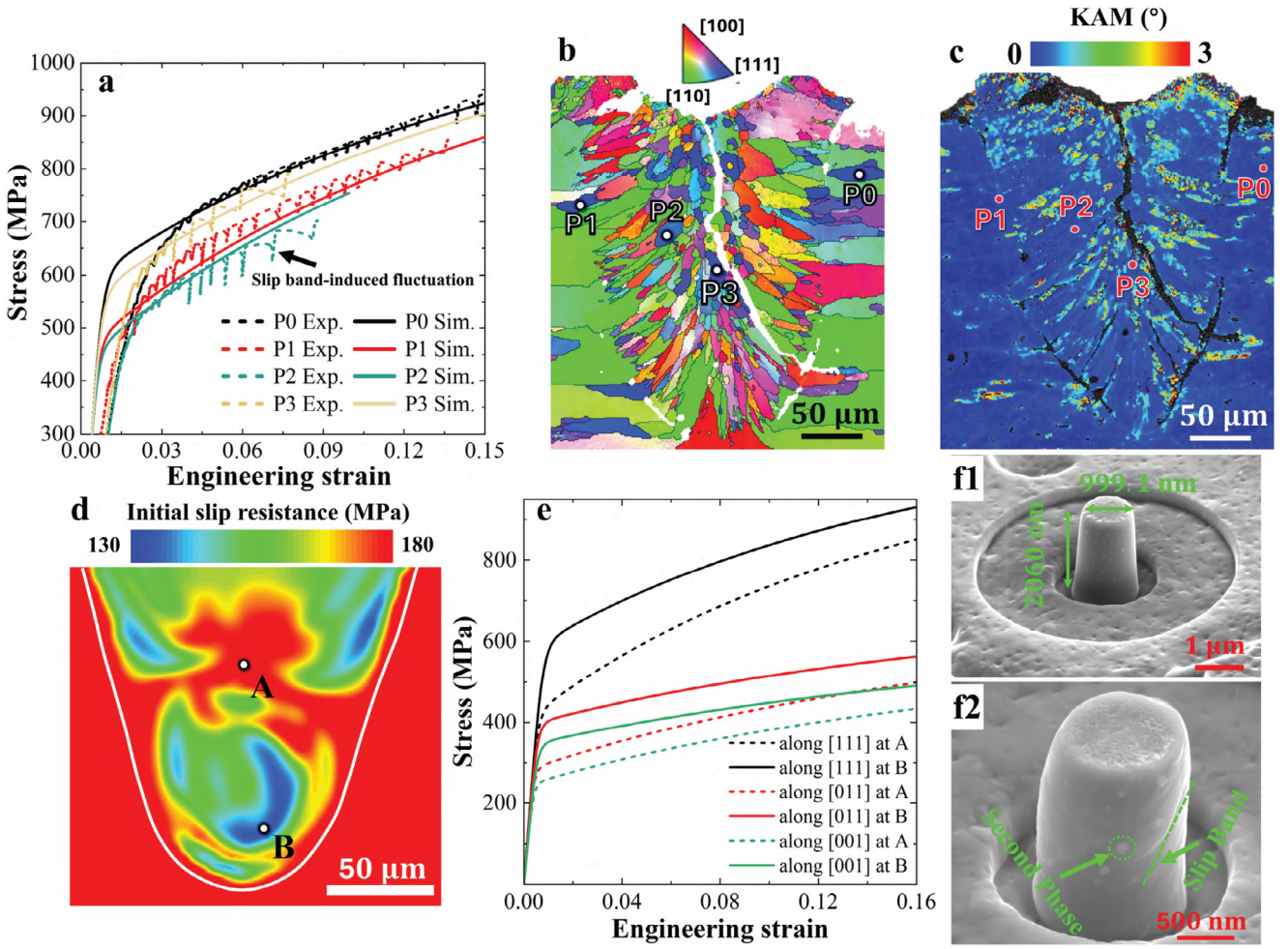

Figure 2. Influence of composition distribution on mechanical properties. a) The strain-stress curves of micro-pillar compression tests at different regions, where P0 is on the substrate and P1-P3 are from the edge to the middle of the melt region as shown in (b). b) EBSD image (IPFZ) of crystal orientation and c) KAM distribution within the cross section of the melt track. The compressive loads are applied along [111] orientation for all P0-P3. d) Simulated initial slip resistance distribution within the cross section of the melt track. e) The simulated stress-strain responses under different crystal orientations and locations marked in (d), in which 0.2% engineering strain is used as the criterion to determine the yield stress. f) SEM images of a micropillar before and after compression tests.

become less evident, indicating that Zn concentration becomes more uniform as the distance to the middle longitudinal section increases. Furthermore, a ripple pattern of Zn concentration, identifiable by the intervals between yellow and red colors in Figure S3c,d (Supporting Information), forms at the middle regions along the laser scanning direction, similar to the ripples distributed on the surface Figure S4e,f (Supporting Information). This cirrus-shaped 3D distribution generally appears in various alloys by L-PBF, as the flow patterns are similar. We also run simulations for L-PBF of a FeMnCoCr high-entropy alloy, which indeed shows such distribution in Figure S7 (Supporting Information).

2.2. Impact of Composition Evolution on Mechanical Property

To assess the impact of element evaporation on the mechanical properties, micro-pillar compression tests are conducted at different locations, as presented in **Figure** 2a. The locations of micropillars are precisely determined based on the Electron Backscatter Diffraction (EBSD) results as shown in Figure 2b and EPMA results. According to the distribution pattern of Zn concentration, P0 is located in the substrate (unmelt region) and serves as the reference point. P1 is at the edge of the melt region, P3 at the bottom of the melt region, and P2 between P1 and P2. In the experiments, the micropillars are prepared after EPMA examination, which is several microns below the cross section in EPMA results. Additionally, the Zn concentration in the EPMA results shows a similar distribution pattern. Consequently, it can be inferred that the Zn concentrations in P1-P3 are 1.0–2.0 wt.% lower than that in the substrate (P0), as shown in Figure 1b. Moreover, the crystal orientations of the pillars align with [111] to exclude the influence of the crystal orientation. Meanwhile, in the compression tests, by extracting P0-P3 (the pillars inside individual grains) with close kernel average misorientations (KAM) (Figure 2c), the influences of initial dislocation hardening on the

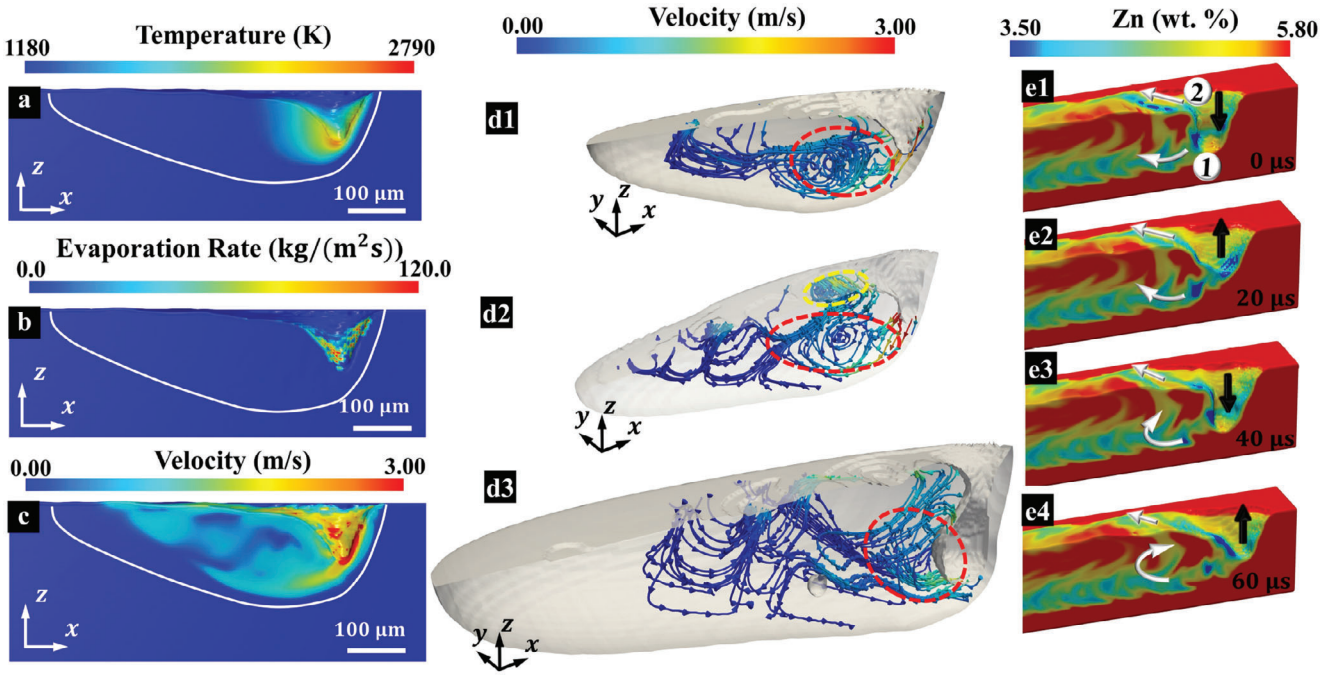

Figure 3. Mechanisms of evaporation-induced composition evolution. Simulation results of a) the temperature, b) evaporation rate on the molten pool surface, c) the velocity magnitudes, d) streamlines, and e) snapshots of Zn evolution in the molten pool during the laser scanning. (a–c, and e) are the simulation results of Case 1, and (d1–d3) are Case 1–3, respectively. The white solid lines in (a–c) and contours in (d) are the boundaries of the molten pool. The black arrow in (e) indicates the keyhole bottom fluctuation direction, and white arrows 1 and 2 indicate the flow direction of low-Zn-concentration fluid in the upper and lower regions of molten pool in Case 1.

stress–strain responses can be excluded. Overall, despite the similarities in the elastic stage for pillars in both the track and substrate, there is a notable reduction in yield strength within the track, particularly at P1 and P2 as shown in Figure 2b. Meanwhile, the yield strength at P3 (bottom region) is ≈100 MPa higher than that at P1 and P2. The significant role of Zn and Mg in augmenting solid-solution strengthening has been well-established[36] and the concentrations of Zn and Mg decrease notably at P1 and P2, and potentially at P3, as illustrated in Figure 1c,d. Thus, the variations in yield strength observed at different positions can be attributed to the disparate concentrations of solid-solution elements.

Furthermore, we use the constitutive model under crystal plasticity (CP) framework to quantify the effect of concentration distributions on stress-strain responses at different locations, in which the solid-solution strengthening effect is incorporated. The stress-strain curves given by experiments are employed for calibrating model parameters, with excellent fitting results shown in Figure 2a. As shown in Figure 2d, the initial slip resistance as a internal state variable in the constitutive model, exhibits a significant non-uniform distribution, which is induced by the segregation of solid-solution elements Zn and Mg. Due to the reduction in solid-solution strengthening induced by element evaporation, the minimum initial slip resistance occurs at depletion regions of Zn and Mg, which is only 66% of that in the substrate. By comparing the mechanical properties at the locations with maximum and minimum initial slip resistance by applying the stress at each location (Figure 2d), this 33% reduction in initial slip resistance can lead to the yield stress decreasing by 98.1 MPa for [001], 112.6 MPa for [110], and 169.8 MPa for [111] orientations, as shown in Figure 1e. Therefore, our simulation framework unveils that evaporation-induced compositional evolution can significantly weaken the slip resistance and yield strength within the fusion zone, and this weakening effect is more pronounced in the depleted regions of Zn and Mg.

2.3. Mechanisms of Composition Evolution

To reveal the formation mechanisms underlying the 3D cirrus-shaped composition distribution, the temperature, local evaporation rate, velocity magnitudes, streamlines, and Zn concentration in the molten pool are presented in **Figure 3**, Figure S8, and Movie S1–S6 (Supporting Information). The composition evolution in the molten pool consists of two parts: element loss through evaporation and element redistribution through liquid convection. The temperature above the Zn boiling point (1180 K) and evaporation rate at the surface in Figure 3a, indicate that the element evaporation concentrates on the keyhole surface non-uniformly (Figure 3b). During the L-PBF process, hydrodynamic and evaporation-induced recoil forces vary across different locations, causing fluctuations of the keyhole surface, which subsequently influence heat convection in the molten pool. Concurrently, the keyhole shape affects the reflection and absorption of the Gaussian-distributed laser.[37] Consequently, keyhole dynamics result in varying temperature distributions, leading to different local evaporation rates on the keyhole surface. Additionally, surface temperatures are lower than Al boiling point (2790 K), so

that the main components of evaporation loss are Zn and Mg elements.

The keyhole fluctuation is intense, with an amplitude of more than 100 µm in-depth and a period less than 10 µs.[25,28] Thus, the low-Zn-concentration keyhole regions (as shown in the keyhole surface of Figure 3e) are either mixed into the bottom region of the molten pool when the keyhole depth increases, or pushed to the rear part of the molten pool as the keyhole surface fluctuates up. During this fierce evaporation and fluctuation process, on the one hand, the vortex at the bottom of the keyhole (Figure 3d) blends the low-Zn-concentration fluid into the molten pool as indicated by Arrow 1 in Figure 3e. On the other hand, the Marangoni effect, caused by the temperature gradient and element concentration difference on the molten pool surface, drives the liquid at the surface around keyhole (low-Zn-concentration region) to the edge of the molten pool as indicated by Arrow 2 in Figure 3e and Movies S1 and S2 (Supporting Information). Additionally, this confines the low-Zn-concentration liquid from the surface in the upper corner as shown in Figure 1c,d,f,g. As the keyhole fluctuates up and down, indicated by the black arrows in Figure 3e, the low-Zn-concentration becomes discontinuous and formulates the 3D cirrus-shaped composition distribution.

Although the streamlines in Figure 3d1 (indicated by the red dashed circles) show that the low-Zn-concentration fluid around the keyhole is moving into the middle of the molten pool for further mixing, the liquid mixing varies with melting mode. In the shallow keyhole mode (Case 1), the streamlines in the molten pool spiral from the front to the rear part, similar to the in situ X-ray imaging results by Guo et al.,[38] With a larger molten pool depth, the spiral streamlines are warped into a vertical vortex behind the keyhole, as shown in Figure 3d2, like the in situ X-ray imaging results by Hojjatzadeh et al.,[26] In Case 3 with an even larger molten pool depth (Figure 3d3), the vertical vortex expands, and liquid flows from the bottom back to the surface of the molten pool with a deeper keyhole. Therefore, as the molten pool depth increases, the expansion of streamlines is responsible for the reduction of Zn segregation levels in the molten pool (Figure 1; Figures S1–S4, Supporting Information) and further influences the shape of the low-Zn-concentration regions.

2.4. Possible Factors Affecting Crack Formation

The OM images in **Figure 4a** show that cracking occurs in the tracks, and previous studies[2,7,39,40] speculated without direct evidence that either thermodynamic conditions or local element concentrations determine the rapid evolution of micro-structures and thus lead to the formation of cracking. Therefore, the temperature gradient, cooling rate, and element concentration distribution and evolution in the molten pool are further analyzed to explore possible causes of cracking. In Figure 4b,c, the temperature gradient and cooling rate within the solidifying regions are alike for all three cases, in the ranges of $10^6 - 10^7$ Km^{-1} and $10^5 - 10^7$ Ks^{-1}, respectively. Generally, high magnitudes of temperature gradient and cooling rate increase the possibility of cracking.[2,7] However, the mechanisms of cracking cannot be fully explained by further comparing the distribution of these two indexes. In Cases 1 and 2, the temperature gradient and cooling rate in Region 2 (bottom region) are higher than those in Region 1 (upper region), as shown in Figure 4b1,b2,c1,c2, while the opposite occurs in Case 3. This implies that cracking should preferentially occur at the bottom of the molten pool in Cases 1 and 2 and at the upper region in Case 3, due to higher thermal stresses proportional to the temperature gradients. However, experimental results (Figure 4a) show that cracks propagate from the bottom of the track, especially in Case 3 where the crack lies in the center of the track vertically and spans from near the bottom to the surface, as indicated in the OM images and revealed by the in situ X-ray images[41,42] in Figure 4d. Meanwhile, some small cracks close to the bottom of the molten pool are found in Case 3 (Figure 4a3) where the Zn concentration around the crack (Figure S2a, Supporting Information) is lower. Thus, other factors significantly affect the formation of cracking and should be taken into account.

As the average keyhole depth increases from Case 1 to 3, the keyhole undergoes intenser fluctuations, resulting in higher possibility of collapsing to form instant bubbles and keyhole pores, which in turn impacts molten pool flow and solidification.[4,25] According to our simulation results, the instant bubble from keyhole collapse can not only lead to keyhole pore defects (Figure S2b, Supporting Information)[25,28] but also obstruct the element convection, as shown in Figure 4e and Movie S7 (Supporting Information). The instant bubble originates at the bottom of the molten pool by the keyhole collapse, where the Zn concentration is low due to the higher element evaporation rate, as displayed in Figure 4e1. As the bubble ascends, the low-Zn-concentration fluid attaches to the bubble, and the liquid convection is hindered. Therefore, the Zn concentration near the solidification front (the gray ellipse region in Figure 4e1–e4) is affected by this instant bubble. As shown in Figure 4e1–e3, Zn concentration at the side of this gray region decreases before increasing, while it behaves oppositely at the bottom of this region. At the same time, the element concentration in the upper region of the molten pool is more uniform than that in the lower region after solidification (Figure 4e5).

This irregular element concentration variation at the bottom of the track during the solidification further impacts grain growth and increases the possibility of cracking. According to thermodynamics, the local element concentration of alloy largely determines Gibbs free energy and impacts the dendrite growth rate.[2] A higher Zn concentration on the solidification front can enhance constitutional supercooling and promote dendritic growth.[43] At the same time, the eutectic temperature of the Al–Cu–Mg ternary system is 698 K (if all Zn element is evaporated), while the solidus temperature of AA7075 is 806 K.[22] Therefore, the change of Zn and Mg concentrations causes variation in both the local solidus temperature and dendrite growth rate. This ever-changing dendrite growth rate could facilitate the formation of interlocking solid networks,[9,44] which increases the potential of cracking. A study on microstructure evolution considering concentration evolution due to evaporation during L-PBF is essential to quantify the potential for crack formation in the future. Thus, the non-uniform and varying composition at the bottom of the molten pool increases the possibility of cracking by changing the local dendrite/grain growth and solidification shrinkage and explains that more cracks appear at the bottom regions of the tracks than at the upper region. Similarly, in situ X-ray imaging[42] and atom probe tomography (APT)[44] results

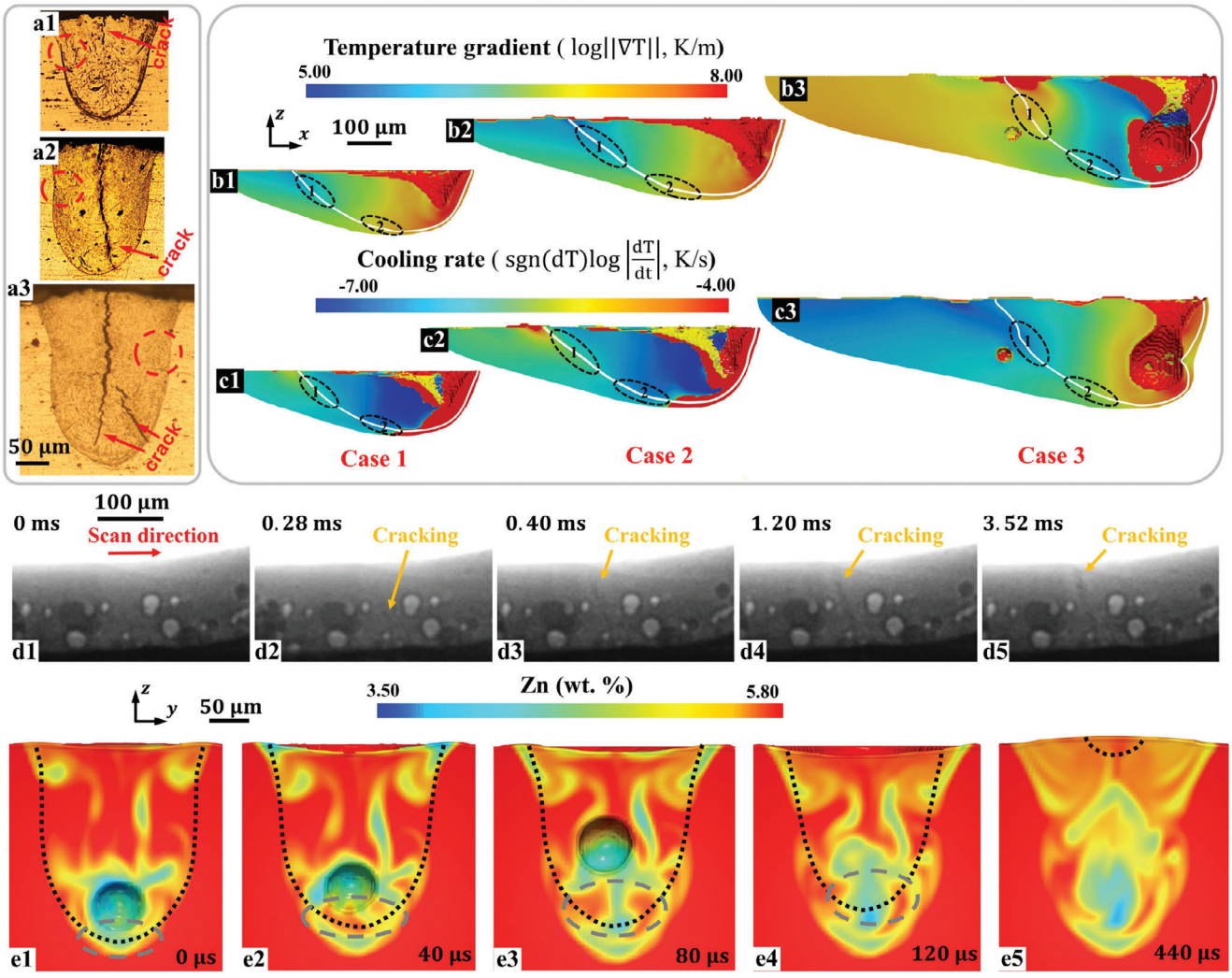

Figure 4. Possible factors affecting cracking formation. a) Metallograph by optical microscope (OM) and cracks are indicated with arrows. The contrast in red circles of OM suggests that element concentrations are segregated into upper and bottom regions in each cross section. The simulation results of b) the temperature gradient, and c) cooling rate in the molten pool. d) In situ X-ray imaging results of cracking propagating from the bottom to the surface of the molten pool during L-PBF.[41] e) The simulated Zn concentration evolution in the molten pool with instant bubble motion. The white solid lines in (b,c) and black dashed lines in (e) indicate the solidification fronts (liquidus temperature). The gray dashed ellipses in (e) indicate the concentration evolution at the bottom of the molten pool. Figure 4d is adapted from Ghasemi-Tabasi H, de Formanoir C, Van Petegem S, et al. Direct observation of crack formation mechanisms with operando Laser Powder Bed Fusion X-ray imaging. Add. Manuf., 2022, 51: 102619, Copyright Elsevier(2022). https://doi.org/10.1016/j.addma.2022.102619. Images were rescaled and their contrast and brightness were adjusted to improve readability.

suggested that instant bubbles in the molten pool increase the possibility of cracking formation and the gas pores could serve as crack nucleation sites and promote crack propagation. Additionally, the pores or cracks (in Figure S2, Supporting Information) in the previous tracks reduce the intensity of molten pool flow and aggravate the local element concentration segregation during the remelting process, Supporting Information.[45] The Zn segregation at the bottom of the molten pool makes the grain morphology more complex, which can further hinder the liquid flow between dendrites. Thus, the liquid convection at the bottom of the molten pool between cracks as shown in Figure 1d and Figures S1 and S2 (Supporting Information) is minimized and leaves a high Zn concentration region at the bottom of the molten pool.

3. Conclusion

In summary, leveraging high-fidelity simulation and detailed experimental characterizations, we have systematically understood the composition evolution caused by evaporative element loss and its impact on mechanical properties. The keyhole fluctuation, Marangoni effect, and different boiling points/evaporation rates of elements lead to the composition variation within the molten pool generally yielding 3D cirrus-shaped distributions. Furthermore, it is possible that the instant bubbles caused by keyhole collapse and keyhole pores hinder liquid convection, exacerbate element segregation, and play critical roles in cracking, aside from the high-temperature gradient and cooling rate, which needs to be validated with more detailed experiments. All these

findings demonstrate that evaporative element loss and the resultant localized variation of mechanical properties are closely related to the manufacturing parameters rather than completely to the chemical compositions of the feedstock material. In future alloy design for MAM, evaporation-induced composition evolution during the manufacturing process should be considered, and integrated design of the raw material compositions and manufacturing parameters is necessary, where computational simulation is a powerful tool to provide guidance.

4. Experimental Section

Multiphysics Thermal-Fluid Flow Model: The metal evaporated from the keyhole surface due to the high-intensity energy input, and the local element concentrations vary due to the different boiling points and evaporation rates of different elements. As the liquid with altered element concentration around the surface was mixed into the molten pool, the element concentrations in the molten pool further changed. To simulate composition evolution and distribution, a compositional evolution model accounting for evaporative elemental loss was developed and integrated with the multiphysics thermal-fluid flow model.[46,47] This model revealed the mesoscale molten pool flow but did not resolve the microscale phase segregation and nanoscale structural evolution during solidification.

In the multiphysics thermal-fluid flow model, the liquid phase is assumed to be an incompressible Newtonian liquid with a constant density (ρ). Taking into account the effects of the mass loss due to evaporation, buoyancy, and drag force in the mushy zone, the mass, momentum, and energy conservation equations are given below

$$\begin{cases} \rho\nabla\cdot\mathbf{u} = \dot{m}_{evp} \\ \rho\dfrac{\partial\mathbf{u}}{\partial t} + \rho\nabla\cdot(\mathbf{u}\otimes\mathbf{u}) = -\nabla p + \mu\nabla^2\mathbf{u} + \mathbf{F}_B - \rho D\mathbf{u} \\ \rho\dfrac{\partial I}{\partial t} + \rho\nabla\cdot(\mathbf{u}I) = \nabla\cdot(k\nabla T) + Q \end{cases} \tag{1}$$

where $\mathbf{u}$ is the velocity vector, $\dot{m}_{evp}$ is the mass loss rate due to the element evaporation, p is the pressure, and T is the temperature. μ and k are the temperature-dependent dynamic viscosity and thermal conductivity of the alloy. $\mathbf{F}_B$ and $D\mathbf{u}$ are the buoyancy based on the Boussinesq approximation and Darcy drag force, respectively. The mushy zone is taken as a porous medium. Based on Darcy's law, the Darcy drag force ($D\mathbf{u}$) is employed to ensure the rigidity and resistance to the flow of the solidified material. The drag coefficient (D) is given by the Blake–Kozeny model[48,49] with the primary dendrite arm spacing taken as 5 µm[50,51] in the current study. In the energy conservation equation, $I = \int C_p(T)\mathrm{d}T + (1-F_s)L_m$ is the specific internal energy, where C_p, L_m, and F_s are the specific heat, latent heat of melting, and solid fraction determined by the temperature. Q is the energy absorbed by the material, which is incorporated by using the ray-tracing method[47,52] to track the multi-reflections of the laser. In the ray-tracing model, the laser is divided into a series of rays, and the laser absorptivity of each ray at each reflection is calculated by the Fresnel equation[23,53] as described in Supporting Information Methods. To track the free surface of the molten pool, the Volume of Fluid (VoF) method[54] is adopted

$$\frac{\partial F}{\partial t} + \nabla\cdot(F\mathbf{u}) = 0 \tag{2}$$

where F is the volume fraction.

Compositional Evolution Model: The alloy system during MAM was taken as a solution, and the solute transport equation for element concentration is

$$\frac{\partial C}{\partial t} + \nabla\cdot(C\mathbf{u}) = \nabla\cdot(D_e\nabla C) + S_v \tag{3}$$

where C is the element concentration in the simulation domain. D_e is the effective diffusion coefficient of the element. S_v is the element concentration loss rate due to the element evaporation,[47,55] which is given as

$$S_v = -\frac{C\dot{m}_{evp} - \dot{m}_{c,i}}{\dot{m}_m - \dot{m}_{evp}} \tag{4}$$

where $\dot{m}_m$ and $\dot{m}_{c,i}$ are the material melting rate and solute evaporating rate of ith element, respectively, and they are calculated with the evaporation model[47] (described in Supporting Information Methods). According to the previous studies,[39,56,57] the diffusion effect in the molten pool dynamics can be ignored compared to the convection effect. The temperature-dependent diffusion coefficient D_e of element in alloy is about $\approx 10^{-7} - 10^{-8}$ $m^2 s^{-1}$ from melting to boiling temperatures.[56,58] In L-PBF process, the characteristic velocity U and length l_c are 2 ms^{-1} and 1 mm, so the Péclet number is $\mathrm{Pe} = Ul_c/D_e \sim 10^4 >> 1$, meaning that the convection is much stronger than diffusion. Thus, the simplified solute transport equation without diffusion is implemented in the current study.

$$\frac{\partial C}{\partial t} + \nabla\cdot(C\mathbf{u}) = S_v \tag{5}$$

In the concentration evolution simulations, the manufacturing parameters were all the same as those in the experiments described in Section Experiments, and the physical properties of AA7075 were calculated with JMatPro and listed in Tables S4 and S5 (Supporting Information). The mesh size was 5 µm to exclude mesh dependence of the simulations. The computation time for a typical case was ≈26 h on a desktop with an Intel i9-12900K CPU. Additionally, this model is also applicable to other materials during MAM and the simulated Mn concentration in L-PBF fabricated FeMnCoCr HEA is validated in Supporting Information Text.

Constitutive Model: In the crystal plasticity framework, the slip rate is given by a power-law relationship[59]

$$\dot{\gamma}^s = \dot{\gamma}_0\left|\frac{\tau^s}{\tau_c^s}\right|^{1/m} sign(\tau^s) \tag{6}$$

where $\dot{\gamma}_0$ is a reference slip rate, τ^s is the resolved shear stress, τ_c^s is the total slip resistance, and m is the exponent of strain rate sensitivity. The total slip resistance can be decomposed into the following terms

$$\tau_c^s = \tau_{PN}^s + \tau_{Oro}^s + \tau_{sol}^s + \tau_{dis}^s \tag{7}$$

where τ_{PN}^s captures the contribution of lattice friction on total slip resistance, τ_{Oro}^s is the contribution of dislocations bypassing of second phase (marked in Figure 2f), τ_{sol}^s is the contribution of solid-solution strengthening, τ_{dis}^s is the contribution of dislocation hardening. Since the slip systems, and the average spacing between adjacent second phases stay the same during deformation, the τ_{PN}^s and τ_{Oro}^s are treated as two constants in this work, which are unified as one constant in the fitting process. Besides, Kalidindi's model was used to describe the evolution of τ_{dis}^s [60]

$$\tau_{dis}^s = \tau_{dis,ini}^s + \Delta\gamma^s q^{\alpha\beta} h_0\left|1 - \frac{\tau_{dis}^s}{\tau_{dis,sat}}\right|^n sign\left(1 - \frac{\tau_{dis}^s}{\tau_{dis,sat}}\right) \tag{8}$$

where $q^{\alpha\beta}$ is a hardening coefficient matrix accounting for the difference in self and latent hardening, h_0 is a constant, $\tau_{dis,\,sat}$ captures the hardening saturation. Furthermore, the τ_{sol}^s is expressed by the concentrations of solid-solution elements, based on the Gypen's model[61]

$$\tau_{sol}^s = \left(\sum_i k_i c_i\right)^p \tag{9}$$

where c_i is the atomic concentration for each solid-solution element (Zn and Mg). The k_i and p are constants that were determined from Ref. [61].

The simulations for mechanical responses were performed under the open-source platform MOOSE.[62] For the simulations in Figure 2a, the simulated element concentrations in Figure 1c,e were taken as the input. The strain rate was set as 0.001 /s, and the compression force was applied along the crystal orientation of [111], which was consistent with the micro-pillar compression tests. The model with calibrated parameters (Table S9, Supporting Information) was employed to map the initial total slip resistance in Figure 2d.

Experiments: The manufacturing parameters for laser scanning and remelting experiments are listed in Table S1 (Supporting Information). 7075-T6 Aluminum Alloy (AA7075) plates were used and the compositions of the plates were measured using inductively coupled plasma optical emission spectrometry (Agilent 730 ICP-OES), as shown in Table S2 (Supporting Information). Before laser scanning, the bare plate was polished to remove the oxide scale and oil stains. The manufacturing chamber was filled with Nitrogen to maintain the Oxygen concentration below 100 ppm at 1 atm and room temperature. The laser scanning was conducted on a BLT-A160 L-PBF machine using a Yb fiber laser with a maximum power of 500 W, a spot size of ≈80 µm, and the wavelength of ≈1.07 µm.

Samples for characterization were obtained from the bare plates using wire electrical discharge machining. After standard metallurgical polishing procedures, the geometrical dimensions of melt track cross sections were measured by an optical microscope (OM, AE2000 MET). The samples for EBSD characterization were prepared by electron-polishing with the solution of 70% methanol and 30% nitric acid at −20 °C after mechanical polishing and the crystal orientations were examined at a step size of 0.5 µm via an Oxford Symmetry EBSD system. In the micro-pillar compression tests, a focused ion beam (FIB) at 30 kV in a FEI-600i dual-beam FIB/SEM system was applied to mill a circle ring with an outer diameter of ≈20 µm, an inner diameter of ≈5 µm, and a depth of ≈0.4 µm in the first step, and then a micro-pillars of roughly 1.0 µm in diameter and 2.0 µm in height were extracted in the inner region.[63] The angle between the compression direction and [111] crystal orientation was smaller than 10° as listed Table S10 (Supporting Information). The micropillars were compressed by a nanoindenter (Hysitron TI 980 TriboIndeter) with a truncated cone tip of 10 µm in diameter. The displacement rate was controlled at 2 nms^{-1} and the strain rate was 1×10^{-3} s^{-1}. Element concentration in the melt tracks was measured by an EPMA (EPMA-1720H) under the conditions of 15 kV, 100 nA, 1.0 µm step size with a counting time of 20 ms per step. The measured Zn concentration in the substrate ranged from 3.0 to 7.0 wt.%. Compared to the ICP-OES results in Table S2 (Supporting Information), the average Zn concentration in the substrate by EPMA is ≈ 0.7 wt.% lower. This discrepancy primarily arose from the presence of an oxidation layer and the inclined surface during the EPMA measurement. In addition to the element segregation due to element evaporation and molten pool flow, the microsegregation of element concentration (phase segregation) during the solidification process can also lead to local variations of element concentration along the grain boundaries. Since the phase segregation and convection of elements occurred separately at the micro and meso scales, a Wiener filter was applied to the EPMA raw data (Figure S9, Supporting Information) to reduce the noise caused by segregation on micro and meso scales (the element segregation on mesoscale in filtered EPMA results still exists) and measurement errors, extracting the features of the Zn evolution results. The chemical composition of the HEA sample was determined using an Oxford Energy Dispersive X-ray Spectroscopy (EDS) detector.

Supporting Information

Supporting Information is available from the Wiley Online Library or from the author.

Acknowledgements

The authors acknowledge the financial support by the Ministry of Education, Singapore, under its Academic Research Fund Tier 2 (MOE-T2EP50221-0013). This research is also supported by A*STAR under its Advanced Models for Additive Manufacturing (AM2) programme (Award M22L2b0111). Any opinions, findings and conclusions or recommendations expressed in this material are those of the author(s) and do not reflect the views of the A*STAR. The authors acknowledge the fruitful discussion inside Dr. Yan's research group, particularly with Dr. Lei Fan and Daijun Hu.

Conflict of Interest

The authors declare no conflict of interest.

Data Availability Statement

The data that support the findings of this study are available from the corresponding author upon reasonable request.

Keywords

additive manufacturing, alloy design, composition evolution, cracking, element evaporation, multiphysics modeling

Received: July 8, 2024
Revised: August 15, 2024
Published online: September 6, 2024

[1] D. Gu, X. Shi, R. Poprawe, D. L. Bourell, R. Setchi, J. Zhu, *Science* **2021**, *372*, eabg1487.
[2] T. DebRoy, H. Wei, J. Zuback, T. Mukherjee, J. Elmer, J. Milewski, A. M. Beese, A. Wilson-Heid, A. De, W. Zhang, *Prog. Mater. Sci.* **2018**, *92*, 112.
[3] D. Herzog, V. Seyda, E. Wycisk, C. Emmelmann, *Acta Mater.* **2016**, *117*, 371.
[4] C. Zhao, B. Shi, S. Chen, D. Du, T. Sun, B. J. Simonds, K. Fezzaa, A. D. Rollett, *Rev. Mod. Phys.* **2022**, *94*, 045002.
[5] I. A. Roberts, C. Wang, R. Esterlein, M. Stanford, D. Mynors, *Int.J. Mach. Tools Manuf.* **2009**, *49*, 916.
[6] Y. Li, D. Gu, *Mater. Des.* **2014**, *63*, 856.
[7] H. Wei, T. Mukherjee, W. Zhang, J. Zuback, G. Knapp, A. De, T. DebRoy, *Prog. Mater. Sci.* **2021**, *116*, 100703.
[8] P. Nie, O. Ojo, Z. Li, *Acta Mater.* **2014**, *77*, 85.
[9] A. Mostafaei, C. Zhao, Y. He, S. R. Ghiaasiaan, B. Shi, S. Shao, N. Shamsaei, Z. Wu, N. Kouraytem, T. Sun, J. Pauza, J. V. Gordon, B. Webler, N. D. Parab, M. Asherloo, Q. Guo, L. Chen, A. D. Rollett, *Curr. Opin. Solid State Mater. Sci.* **2022**, *26*, 100974.
[10] S. Wang, J. Ning, L. Zhu, Z. Yang, W. Yan, Y. Dun, P. Xue, P. Xu, S. Bose, A. Bandyopadhyay, *Mater. Today* **2022**, *59*, 133.
[11] J. Liu, P. Wen, *Mater. Des.* **2022**, *215*, 110505.
[12] V. Juechter, T. Scharowsky, R. Singer, C. Körner, *Acta Mater.* **2014**, *76*, 252.
[13] T. Qi, H. Zhu, H. Zhang, J. Yin, L. Ke, X. Zeng, *Mater. Des.* **2017**, *135*, 257.
[14] L. Zhuo, B. Song, R. Li, Q. Wei, C. Yan, Y. Shi, *Opt. Laser Technol.* **2020**, *127*, 106164.

[15] J. B. Seol, J. W. Bae, J. G. Kim, H. Sung, Z. Li, H. H. Lee, S. H. Shim, J. H. Jang, W.-S. Ko, S. I. Hong, H. S. Kim, *Acta Mater.* **2020**, *194*, 366.
[16] F. Haftlang, H. S. Kim, *Mater. Des.* **2021**, *211*, 110161.
[17] C. Wang, X. Tan, Z. Du, S. Chandra, Z. Sun, C. Lim, S. Tor, C. Lim, C. Wong, *J. Mater. Process. Technol.* **2019**, *271*, 152.
[18] D. Ren, H. Zhang, Y. Liu, S. Li, W. Jin, R. Yang, L. Zhang, *Mater. Sci. Eng., A* **2020**, *771*, 138586.
[19] S. Shiva, I. Palani, S. Mishra, C. Paul, L. Kukreja, *Opt. Laser Technol.* **2015**, *69*, 44.
[20] K. Wei, Z. Wang, X. Zeng, *Mater. Lett.* **2015**, *156*, 187.
[21] J. Schwerdtfeger, C. Körner, *Intermetallics* **2014**, *49*, 29.
[22] W. Stopyra, K. Gruber, I. Smolina, T. Kurzynowski, B. Kuźnicka, *Addit. Manuf.* **2020**, *35*, 101270.
[23] Y. Huang, T. G. Fleming, S. J. Clark, S. Marussi, K. Fezzaa, J. Thiyagalingam, C. L. A. Leung, P. D. Lee, *Nat. Commun.* **2022**, *13*, 1170.
[24] Z. Zhu, Z. Hu, H. L. Seet, T. Liu, W. Liao, U. Ramamurty, S. M. Ling Nai, *Int. J. Mach. Tools Manuf.* **2023**, *190*, 104047.
[25] C. Zhao, N. D. Parab, X. Li, K. Fezzaa, W. Tan, A. D. Rollett, T. Sun, *Science* **2020**, *370*, 1080.
[26] S. M. H. Hojjatzadeh, N. D. Parab, W. Yan, Q. Guo, L. Xiong, C. Zhao, M. Qu, L. I. Escano, X. Xiao, K. Fezzaa, W. Everhart, T. Sun, L. Chen, *Nat. Commun.* **2019**, *10*, 3088.
[27] L. Wang, Q. Guo, L. Chen, W. Yan, *Int. J. Mach. Tools Manuf.* **2023**, *193*, 104077.
[28] L. Wang, Y. Zhang, H. Y. Chia, W. Yan, *npj Comput. Mater.* **2022**, *8*, 22.
[29] S. A. Khairallah, A. T. Anderson, A. Rubenchik, W. E. King, *Acta Mater.* **2016**, *108*, 36.
[30] M. Yang, L. Wang, W. Yan, *npj Comput. Mater.* **2021**, *7*, 1.
[31] J. H. Martin, B. D. Yahata, J. M. Hundley, J. A. Mayer, T. A. Schaedler, T. M. Pollock, *Nature* **2017**, *549*, 365.
[32] P. A. Rometsch, Y. Zhu, X. Wu, A. Huang, *Mater. Des.* **2022**, *219*, 110779.
[33] R. J. Hebert, *J. Mater. Sci.* **2016**, *51*, 1165.
[34] I. F. Bainbridge, J. A. Taylor, *Metall. Mater. Trans. A* **2013**, *44*, 3901.
[35] L. Yao, Z. Xiao, Z. Hoo, C. Tang, J. Qiao, Y. Zhang, *Mater. Res. Lett.* **2023**, *11*, 814.
[36] M. Bignon, Z. Ma, J. D. Robson, P. Shanthraj, *Acta Mater.* **2023**, *247*, 118735.
[37] S. A. Khairallah, A. A. Martin, J. R. Lee, G. Guss, N. P. Calta, J. A. Hammons, M. H. Nielsen, K. Chaput, E. Schwalbach, M. N. Shah, M. G. Chapman, T. M. Willey, A. M. Rubenchik, A. T. Anderson, Y. M. Wang, M. J. Matthews, W. E. King, *Science* **2020**, *368*, 660.
[38] Q. Guo, C. Zhao, M. Qu, L. Xiong, S. M. H. Hojjatzadeh, L. I. Escano, N. D. Parab, K. Fezzaa, T. Sun, L. Chen, *Addit. Manuf.* **2020**, *31*, 100939.
[39] J. Shinjo, A. Kutsukake, A. Arote, Y. T. Tang, D. G. McCartney, R. C. Reed, C. Panwisawas, *Addit. Manuf.* **2023**, *64*, 103428.
[40] P. Kontis, E. Chauvet, Z. Peng, J. He, A. K. da Silva, D. Raabe, C. Tassin, J.-J. Blandin, S. Abed, R. Dendievel, B. Gault, G. Martin, *Acta Mater.* **2019**, *177*, 209.
[41] H. Ghasemi-Tabasi, C. de Formanoir, S. Van Petegem, J. Jhabvala, S. Hocine, E. Boillat, N. Sohrabi, F. Marone, D. Grolimund, H. Van Swygenhoven, R. E. Logé, *Addit. Manuf.* **2022**, *51*, 102619.
[42] Y. Chen, D. Zhang, P. O'Toole, D. Qiu, M. Seibold, K. M. Schricker, J. P. Bergmann, A. Rack, M. Easton, *Comm. Mater.* **2023**, *5*, 84.
[43] K. Wang, Y. Chen, X. Dou, Y. Han, *Adv. Powder Technol.* **2021**, *32*, 1766.
[44] Z. Sun, Y. Ma, D. Ponge, S. Zaefferer, E. A. Jägle, B. Gault, A. D. Rollett, D. Raabe, *Nat. Commun.* **2022**, *13*, 4361.
[45] S. M. H. Hojjatzadeh, N. D. Parab, Q. Guo, M. Qu, L. Xiong, C. Zhao, L. I. Escano, K. Fezzaa, W. Everhart, T. Sun, L. Chen, *Int. J. Mach. Tools Manuf.* **2020**, *153*, 103555.
[46] W. Yan, W. Ge, J. Smith, S. Lin, O. L. Kafka, F. Lin, W. K. Liu, *Acta Mater.* **2016**, *115*, 403.
[47] L. Wang, Y. Zhang, W. Yan, *Phys. Rev. Appl.* **2020**, *14*, 064039.
[48] D. R. Poirier, *Metall. Trans. B* **1987**, *18*, 245.
[49] C. Amador, L. M. de Juan, in *Computer Aided Chemical Engineering*, vol. *39*, Elsevier, Amsterdam **2016**, pp. 509–579.
[50] S. Sampath, H. Herman, *J. Therm. Spray Technol.* **1996**, *5*, 445.
[51] M. C. Flemings, Y. Shiohara, *Mater. Sci. Eng.* **1984**, *65*, 157.
[52] J. Ahn, S.-J. Na, *Appl. Surf. Sci.* **2013**, *283*, 115.
[53] A. Mahrle, E. Beyer, *J. Phys. D: Appl. Phys.* **2009**, *42*, 175507.
[54] C. W. Hirt, B. D. Nichols, *J. Comput. Phys.* **1981**, *39*, 201.
[55] A. Klassen, V. E. Forster, V. Juechter, C. Körner, *J. Mater. Process. Technol.* **2017**, *247*, 280.
[56] F. Van Loo, G. Rieck, *Acta Metall.* **1973**, *21*, 61.
[57] H. Nakajima, M. Koiwa, *ISIJ Int.* **1991**, *31*, 757.
[58] H. Lu, G. Li, Y. Zhu, Q. Jiang, *J. Non-Cryst. Solids* **2006**, *352*, 2797.
[59] S. R. Kalidindi, C. A. Bronkhorst, L. Anand, *J. Mech. Phys. Solids* **1992**, *40*, 537.
[60] S. R. Kalidindi, *Int. J. Plast.* **2001**, *17*, 837.
[61] L. Gypen, A. Deruyttere, *J.Less-Common Met.* **1977**, *56*, 91.
[62] A. D. Lindsay, D. R. Gaston, C. J. Permann, J. M. Miller, D. Andrš, A. E. Slaughter, F. Kong, J. Hansel, R. W. Carlsen, C. Icenhour, L. Harbour, G. L. Giudicelli, R. H. Stogner, P. German, J. Badger, S. Biswas, L. Chapuis, C. Green, J. Hales, T. Hu, C. Wong, *SoftwareX* **2022**, *20*, 101202.
[63] X. Bian, G. Wang, H. Chen, L. Yan, J. Wang, Q. Wang, P. Hu, J. Ren, K. C. Chan, N. Zheng, A. Teresiak, Y. L. Gao, Q. J. Zhai, J. Eckert, J. Beadsworth, K. A. Dahmen, P. K. Liaw, *Acta Mater.* **2016**, *106*, 66.